

## Equatorial Undercurrent and North Equatorial Countercurrent at 38°W: A new perspective from direct velocity data

D. F. Urbano,<sup>1</sup> R. A. F. De Almeida,<sup>1</sup> and P. Nobre<sup>1</sup>

Received 13 March 2007; revised 31 October 2007; accepted 28 December 2007; published 30 April 2008.

[1] The western Equatorial Undercurrent (EUC) and North Equatorial Countercurrent (NECC) are investigated at 38°W using contemporaneous subsurface (ADCP) and high-resolution near-surface (drifters + satellite altimeter) velocity measurements, together with hydrographic (CTDO<sub>2</sub>) data that were collected from 1998 to 2006. The observations reveal an EUC with a strong semiannual pattern of intensification. Direct measurements also confirm the existence of a northern branch of the NECC (nNECC), observed here for the first time in the western tropical Atlantic. The NECC displays an annual cycle of northward migration on the basin, driven by the Sverdrup transport generated by the wind field. In this cycle the nNECC is a semipersistent feature fed by waters from the Northern Hemisphere and the residual nNECC flow from the previous year.

**Citation:** Urbano, D. F., R. A. F. De Almeida, and P. Nobre (2008), Equatorial Undercurrent and North Equatorial Countercurrent at 38°W: A new perspective from direct velocity data, *J. Geophys. Res.*, 113, C04041, doi:10.1029/2007JC004215.

### 1. Introduction

[2] In the tropical Atlantic Ocean, separating the oppositely rotating North and South Atlantic gyres, a dynamically complex system of currents flows mainly in the zonal direction (Figure 1). The westward North and South Equatorial Currents (NEC and SEC), which are the equatorward arms of the subtropical gyres, are separated by the eastward Equatorial Undercurrent (EUC), North Equatorial Countercurrent (NECC), and North Equatorial Undercurrent (NEUC). While the NEUC is always above the thermocline and has a weak seasonal cycle, the variability of EUC and of the NECC is mainly driven by the wind field over the whole tropical basin, displaying a strong annual pattern of interaction with the atmosphere. The understanding of the structure and variability of these two currents is crucial for studies concerning the coupled ocean-atmosphere interaction in the region.

[3] The eastward currents in the tropical Atlantic are fed predominantly by waters from the North Brazil Current (NBC), when this strong current crosses the equator and, because of conservation of vorticity, retroflects and feeds in different vertical levels the EUC, the NEUC, and the NECC. The NBC originates from the North Brazil Undercurrent (NBUC), a northward flow along the coast of Brazil between 5°S and 10°S into the western boundary [Silveira *et al.*, 1994; Schott *et al.*, 1995; Stramma and Schott, 1999]. This current is fed by waters from the southeast and central South Atlantic originated by the bifurcation of the southern branch of the South Equatorial Current (sSEC), south of

15°S. After turning around Cape Sao Roque, the NBUC is overlaid by waters from the eastern part of the basin that are carried by the surface-intensified central South Equatorial Current (cSEC). The NBUC loses its undercurrent character and becomes the NBC [Schott *et al.*, 1998]. An important consequence of the NBC retroflexion is that the barotropically unstable NECC generates Rossby waves of the first baroclinic mode, which reflect at the South American coast creating 6–7 anticyclones per year that intensify and become NBC rings [Jochum and Malanotte-Rizzoli, 2003]. The rings shed by the retroflexion propagate northwestward along the Guyana coast, exporting heat toward the North Atlantic [Didden and Schott, 1993; Wilson *et al.*, 2002].

[4] In both off-equatorial hemispheres, the unbalance between evaporation and precipitation imposed by the surface winds in the subtropical regions generates oxygen-rich and saltier (denser) waters that sink and flow equatorward in pycnocline levels, ventilating the tropical thermocline before rising in the equatorial upwelling along the EUC. Back in the surface, these waters flow poleward driven by the surface Ekman drift, closing the so-called Subtropical-Tropical Cells (STCs; Stramma and Schott [1999]; Snowden and Molinari [2003]). In the North Hemisphere, three different subduction windows exist in the off-equatorial zone, each one connecting the subtropics with the equatorial region through a different root. These pathways were demonstrated by model results [Malanotte-Rizzoli *et al.*, 2000; Lazar *et al.*, 2002; Inui *et al.*, 2002] and by climatological observations [Zang *et al.*, 2003]. The main path from the North Atlantic waters into the equatorial region is through the Guyana Undercurrent (GUC; Wilson *et al.* [1994]), which is the southeastward coastal undercurrent at northwest of the NBC retroflexion region. It was shown by Bourlès *et al.* [1999a] that the NEUC and NECC are fed by the GUC (referred by the authors as Western Boundary Undercurrent

<sup>1</sup>Divisão de Modelagem e Desenvolvimento, Centro de Previsão de Tempo e Estudos Climáticos, Instituto Nacional de Pesquisas Espaciais, Cachoeira Paulista, São Paulo, Brazil.

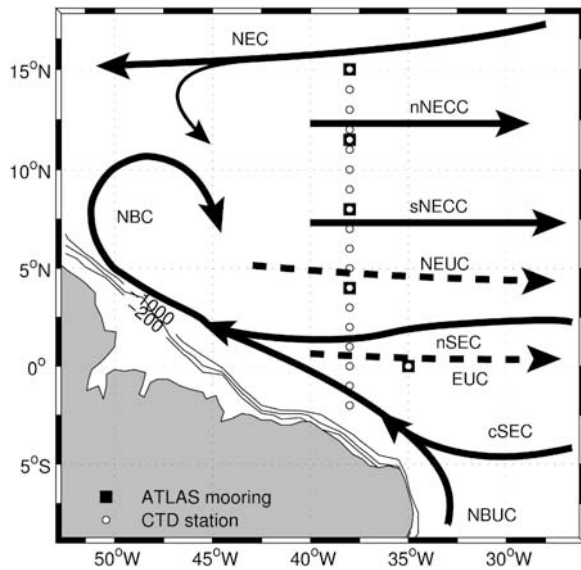


**Figure 1.** Schematic upper ocean circulation in the western tropical Atlantic. Superimposed are the western PIRATA array with the ATLAS moorings (squares) and CTD stations along 38°W (circles). The contours show the 200-, 500-, and 1000-m isobaths.

(WBUC)), but no observational evidence was presented for North Atlantic waters in the EUC, as suggested by numerical experiments [Schott and Böning, 1991]. How the oxygen-rich and saltier waters leave the GUC to feed the EUC, if do so, is still an open question.

[5] Even though intensely investigated, the structure and variability of the EUC and NECC still remain unclear. Schott *et al.* [1995] describe two eastward cores in the EUC at 40°W during March 1994 (Meteor cruise M27). Comparing transports, the authors show that the transport at 44°W and 40°W (14.5 Sv) are almost the same at 35°W (13.7 Sv). On the basis of transport alone, but supported by oxygen analysis of Metcalf and Stalcup [1967], it was shown that the EUC was carrying waters from South Hemisphere only, supplied by the NBC retroflection. On the other hand, in the observational work of Goes *et al.* [2005], the authors examined vertical velocity sections at 44°W, 41°W, and 35°W from a cruise conducted in February 2002, and demonstrated that the single EUC core at 44°W and 41°W separates into the NEUC and EUC by 35°W, with the former composed of northern hemisphere waters and the latter of southern hemisphere waters. Bourlès *et al.* [1999a] also describe two EUC cores from a cruise in March 1994 (CITHER-2). However, owing to the different longitudinal locations of these cores and the 2-d lag between the measurements, it was interpreted as a signature of the EUC meandering behavior. While observational velocity maps show a complex EUC core structure, numerical model outputs of coarse resolution (1/4°) still represent the EUC as an idealized one-core undercurrent. Nevertheless, the only way to understand the EUC seasonal cycle over the basin is using numerical modeling. Arhan *et al.* [2006] analyze the annual cycle of the EUC using a realistic ocean general circulation model and compare the results with observations. The authors describe two well defined transport maxima along the year: one during summer

and fall and a second, most pronounced near the western boundary, during April–May.

[6] The NECC is the major component of the zonal current system and plays a vital role in modulating heat flux through the tropical Atlantic [Philander and Pacanowski, 1986]. Because of its meandering character, it is difficult to determine the meridional limits of the NECC. Inverted Echo Sounders (IES) installed along 28°W and 38.5°W showed that the NECC was located between 3 and 9°N [Garzoli and Richardson, 1989; Garzoli, 1992]. Historic ship drift data were used to define the NECC lying between 3 and 10°N, in the region of 35–45°W [Richardson and McKee, 1984]. Fonseca *et al.* [2004] confirmed these latitudinal limits through a combination of altimeter-derived sea height anomalies and climatological hydrographic data. The authors also conclude that the NECC's location closely follows the annual migration of the ITCZ except during February (time in which the ITCZ is far south), when this current exhibits a secondary northward maximum. More recently, Lumpkin and Garzoli [2005], through time-mean surface direct velocity measurements (drifters), describe the NECC as an eastward component across the entire basin, from the mean NBC retroflection at 5–8°N, 45–50°W to the Guinea Current at 2–4°N, 10–15°W.

[7] Urbano *et al.* [2006], through a combination of theory, numerical model outputs, and observations at 35°W, showed a more complex behavior of the NECC. The authors conclude that the NECC is composed by a two-core structure that remains throughout the year and lies between 3°N and 13°N. They showed that these features, in Sverdrup balance, are generated by the particular structure of the Atlantic wind field (e.g., ITCZ). Recent direct velocity data in the eastern Atlantic [Stramma *et al.*, 2005a] confirm the NECC double-core existence, while in the western part of the basin only few direct velocity measurements were conducted north of 5°N, and none north of 7.5°N.

[8] Motivated by the statements presented above, the main objective of this work is to investigate the structure and variability of the NECC and EUC at 38°W using high-resolution near-surface and subsurface direct velocity measurements. Our focus is mainly in the large-scale flow field, therefore nonlinear dynamics and mesoscale eddy activity, even though important, will not be deeply discussed here. The text is organized as follows: section 2 describes the data sets used in this paper. Section 3 presents the main results, including a discussion of the water masses, a description of the velocity field and an analysis of the variability at 38°W. The discussion, in section 4, is followed by a summary and conclusions in section 5.

## 2. Data

[9] Two different data sets that cover the period of 1998 to 2006 are used in this study: ship data from the Pilot Research Moored Array in the tropical Atlantic (PIRATA), a multinational cooperative program [Servain *et al.*, 1998], and a combination of drifter data from the Surface Velocity Program (SVP) with satellite altimeter data from CNES/Aviso (Archiving, Validation, and Interpretation of Satellite Oceanographic data) [Niiler *et al.*, 2003].

**Table 1.** Summary of Brazilian PIRATA Cruises, Dates, and ADCP/CTD Data Types

Cruise	Alias	Boreal Season	Section	Data Type
PIRATA BR I <sup>a</sup>	JAN1998	winter	15°N–4°N, 38°W	CTD
PIRATA BR II	FEB1999	winter	15°N–3°S, 38°W	Transect/CTD
PIRATA BR III	MAR2000	winter	15°N–2°S, 38°W	Transect/CTD
PIRATA BR IV	APR2001	spring	15°N–3°S, 38°W	VM-DAS/CTD
PIRATA BR V <sup>a</sup>	APR2002	spring	15°N–3°S, 38°W	VM-DAS/CTD
PIRATA BR VI	JUL2003	summer	15°N–3°S, 38°W	VM-DAS/CTDO <sub>2</sub>
PIRATA BR VII	JUL2004	summer	15°N, 38°W–3°S, 35°W	VM-DAS/CTDO <sub>2</sub> <sup>b</sup>
PIRATA BR VIII	JUL2005	summer	15°N–2°S, 38°W	VM-DAS/CTDO <sub>2</sub> <sup>b</sup>

<sup>a</sup>Will not be used here.<sup>b</sup>CTDO<sub>2</sub> at ATLAS sites only.

## 2.1. Subsurface Velocity and Water Mass Properties

[10] Since 1998, oceanographic annual surveys have been conducted by the PIRATA Brazilian effort for maintenance of the Autonomous Temperature Line Acquisition System (ATLAS) moorings (Figure 1). Underway shipboard Acoustic Doppler Current Profiler (ADCP) data were collected, Conductivity-Temperature-Depth (CTD) instruments were cast, and Expendable Bathythermograph (XBT) probes were released. The CTD locations for the seven cruises considered herein are shown in Figure 1. The tracks, dates, and data types for each cruise are summarized in Table 1.

### 2.1.1. Shipboard ADCP

[11] Upper ocean velocity was measured by a 75-kHz vessel-mounted ADCP from RD Instruments on board the Brazilian Navy R/V Antares. The data were collected continuously along the ship tracks. The track lines changed from year to year since the sequence of moorings to be visited is dependent on weather conditions.

[12] The seven PIRATA ADCP data sets were named Transect or VM-DAS according to the employed data acquisition software (Table 1). The raw data were collected using a vertical bin length of 8 m with the first reliable bin representing a velocity mean from 16 to 24 m in depth. Because of an unfortunate hull shape and no acoustic window installed on the profiler, the downward acoustic bin penetration was always shallower than the instrument nominal range of 800 m. The depth range was about 450–500 m but it is dependent on sea state; the range was less than 200 m when the ship headed into heavier weather. Depending on the season, a combination of the strength of the trades, waves, and surface currents increase the ship instability, drastically affecting the acoustic penetration, which in this case reaches roughly 50-m depth.

[13] The ADCP data were processed and calibrated using the Common Ocean Data Access System (CODAS) developed and maintained by the University of Hawaii [Firing *et al.*, 1995]. The original 10-min mean values have been processed using only values over 50 percent good and further averaged into 1/4° horizontally. Absolute current velocity was determined by using standard shipboard gyroscopic compass heading and navigation from the Global Positioning System (GPS), with a synchronization ratio of 1:1. The orientation of the transducer relative to the gyroscopic compass and an amplitude correction factor for the ADCP were determined by standard calibration procedures [Joyce, 1989; Pollard and Read, 1989].

[14] The accuracy of the mean velocity profiles was evaluated using the CODAS software quality tools [Firing *et al.*, 1995]. The maximum error velocity found was from 1.5 to 2.5 cm s<sup>−1</sup> for all cruises but APR2002. The

mean profile of error velocity for this cruise showed peaks of 5 cm s<sup>−1</sup> and therefore its velocity data was not used. As discussed by Wilson *et al.* [1994], after processing, some error may still remain.

[15] The ADCP data used here are novel observations in the western tropical Atlantic since the track lines reach 15°N. A large number of invaluable ADCP measurements were collected along 38°W and 35°W, but they extended only up to 5°N [Wilson *et al.*, 1994; Schott *et al.*, 2003], or up to 7.5°N [Arhan *et al.*, 1998; Bourlès *et al.*, 1999a, 1999b, 2002]. To the best of our knowledge, there are no ADCP measurements north of 7.5°N at 38°W.

### 2.1.2. CTD and O<sub>2</sub>

[16] Hydrographic data were collected with a SeaBird SBE 9Plus CTD instrument. The conductivity, pressure, temperature, and dissolved oxygen sensors were calibrated in the laboratory prior to each cruise. Duplicity of sensors was used as a mean of quality control, and water samples collected concurrently with the CTD data were only used to provide additional calibration if suspicious data occurred. Dissolved oxygen was also computed from the water samples using the Winkler method described at Grasshoff *et al.* [1983]. Only dissolved oxygen data of the JUL2003 cruise were used here because of the correct operation of sensor and high enough horizontal resolution. Temperature, conductivity, pressure, and dissolved oxygen accuracy (resolution) are ±0.004 (0.0003) °C, ±0.002 (0.0004) mS/cm, ±0.02 (0.001) %, and 2% of saturation. Details about the CTDO<sub>2</sub> data reduction and accuracy are provided by the Brazilian Navy cruise reports [DHN, 2005].

[17] From FEB1999 to JUL2003, the measurements were collected at each degree of latitude from 2°S to 15°N, while during JUL2004 and JUL2005 the CTD stations were restricted to the ATLAS positions only (Figure 1).

[18] The CTD stations along 38°W were done either during the northward or the southward cruise tracks. As discussed above, ADCP velocity maps during both sections (southward and northward) are not available. Therefore, matching the velocity section with the CTD was only possible during APR2002 and JUL2003.

### 2.1.3. Density Surfaces

[19] The vertical maps description will be presented mostly in two layers on the basis of the current distribution associated with the density structures, similar to the previous studies of Wilson *et al.* [1994], Schott *et al.* [1995], and Bourlès *et al.* [1999a]. While the SEC, NBC, NEC, and NECC commonly exhibit velocity cores near the surface, the EUC, NEUC, and NBUC velocity cores are found within and below the thermocline [Bourlès *et al.*, 1999a]. For easier comparison with earlier studies, the upper layer is bounded



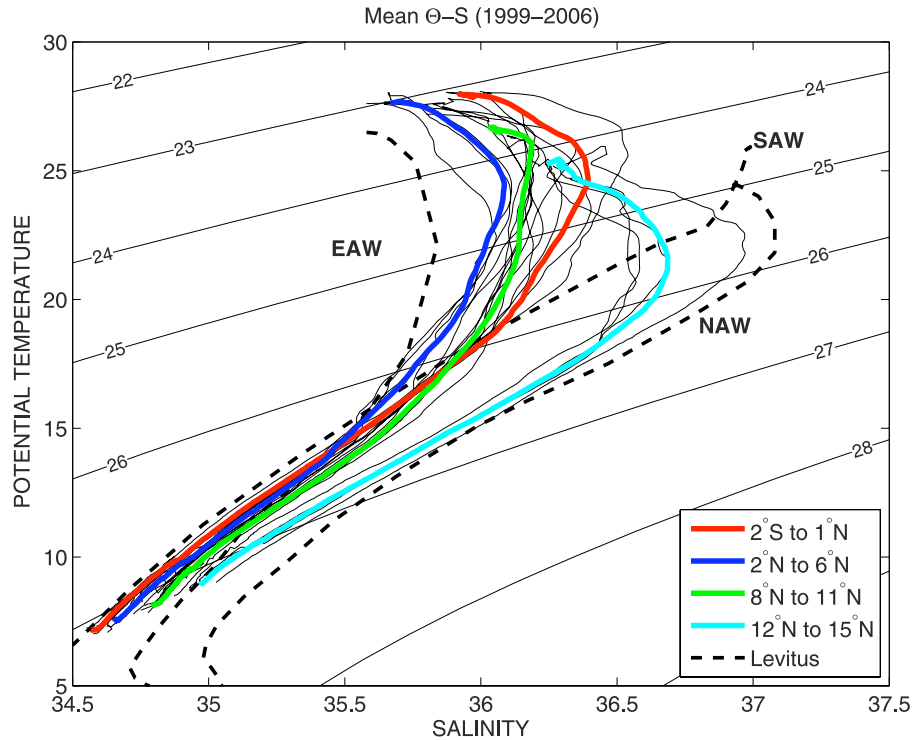


**Figure 2.** Diagram of potential temperature and salinity ( $\Theta$ -S) using all CTD stations collected from 1999 to 2006 at each degree of latitude along 38°W (thin black lines) and mean latitudinal values (colored lines). Levitus climatological profiles (dashed lines) were used as a reference for North Atlantic Water (NAW; 35°W, 15–25°N), Eastern Atlantic Water (EAW; 23°W, 3–15°N), and South Atlantic Water (SAW; 30°W, 15–25°S).

by the sea surface and the isopycnal of  $\sigma_\Theta = 24.5 \text{ kg m}^{-3}$  and the lower layer is bounded by the  $\sigma_\Theta = 24.5 \text{ kg m}^{-3}$  and  $\sigma_\Theta = 26.8 \text{ kg m}^{-3}$  (for brevity, the units will be suppressed from here on). For water mass analysis purposes, the Intermediate Layer is between the  $\sigma_\Theta$  surfaces of 26.8 and 27.1 [Stramma and Schott, 1999].

## 2.2. Near-Surface Velocity

[20] The high-resolution near-surface (Ekman-removed) velocity data for the tropical Atlantic is a data set maintained by the Drifter Data Center at the Atlantic Oceanographic and Meteorological Laboratory of National Oceanic and Atmospheric Administration (AOML/NOAA), kindly made available by Dr. Rick Lumpkin from the Physical Oceanography Division. The synthesis of the data for the tropical Atlantic follows the procedure described in Niiler *et al.* [2003] for the Kuroshio region, and is briefly described below.

[21] The direct velocity data are derived from a large number of drifters that were deployed in or drifted to the tropical Atlantic domain (24°S–24°N, 70°W–14°E) in the period from 07 January 1998 to 20 September 2006 (Rick Lumpkin, personal communication, 2007). The ARGOS location data were processed into 6-hourly estimates of position and velocity by kriging [Hansen and Poulain, 1996]. During each 6-h segment, the NCEP/NCAR reanalysis 6-hourly surface wind vector was interpolated to the drifter location. These wind data were used to correct the 6-h drifter velocity for a wind slip, and additional bias correction was added. To obtain ensemble means, the drifter

velocity is binned and ensemble averaged on two spatial scales. Within each bin, all data are first averaged in time over a 7 d window and then ensemble averaged. The averages over the tropical Atlantic were derived from bins on a  $1/3^\circ$  resolution. The sea level field provided by Aviso is on a two-dimensional  $0.25^\circ$  grid, every 10 d. A geostrophic current was computed from center differencing the data in space, linearly interpolating in time to every 6 h on to the location of the drifter tracks and then binning and averaging over 7 d exactly like the drifter data to produce contemporaneously sampled velocity fields. A geostrophic velocity component was computed from drifter data by subtracting the Ekman current estimated from NCAR/NCEP Reanalysis data set.

## 3. Results

### 3.1. Water Masses

[22] A mean  $\Theta$ -S diagram was built up using the CTD casts collected from 1999 to 2006 along 38°W (Figure 2). Mean values of potential temperature ( $\Theta$ ) and salinity from Levitus climatology [Levitus *et al.*, 1994] were used as reference for the South Atlantic waters (SAW; 30°W, 15–25°S), North Atlantic waters (NAW; 35°W, 15–25°N), and for the Eastern Atlantic waters (EAW; 23°W, 3–15°N). NAW dominates the region north of 11°N, with low mixing rates at 15°N. SAW concentrates south of 2°N, while the mean curve of 2°N to 6°N (Figure 2, dark blue curve) shows the presence of the EAW in the region. From 8°N to 11°N, the  $\Theta$ -S shows mixed values of SAW and EAW. However,

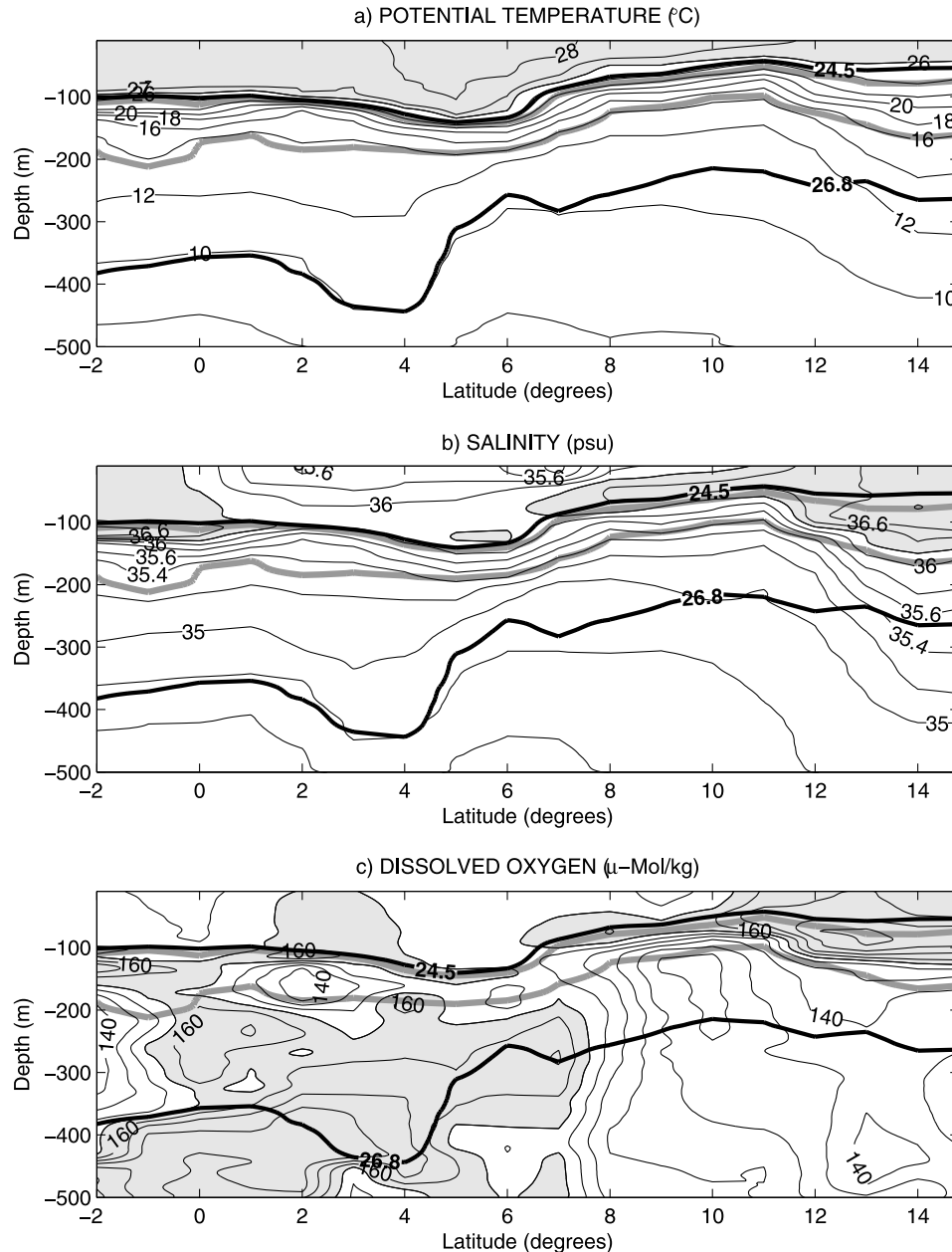


**Figure 3.** Vertical maps of (a) potential temperature, (b) salinity, and (c) dissolved oxygen collected at each degree of latitude during JUL2003 cruise. Gray shades are temperature over 26°C, salinity over 36 psu, and dissolved oxygen over 155  $\mu\text{-Mol kg}^{-1}$ . Superimposed are the potential density ( $\sigma_\theta$ ) of 24.5 and 26.8  $\text{kg m}^{-3}$  (black thick lines), and 25 and 26.5  $\text{kg m}^{-3}$  (gray thick lines).

from temperature and salinity only it is not possible to infer whether the NAW contributes to this mixed water or not.

[23] Different water masses are well identified along 38°W. The Tropical Surface Water (TSW), with temperatures warmer than 26°C, forms the mixed layer of the tropical Atlantic [Csanady, 1987; Stramma *et al.*, 2005b]. In the vertical distribution of potential temperature collected in JUL2006 (Figure 3a), the TSW is located above  $\sigma_\theta$  of 24.5.

[24] The northernmost mean  $\Theta$ -S curve (12–15°N; Figure 2, light blue curve) shows the maximum salinity values of the 38°W section at  $\sigma_\theta = 25.5$ . This feature is the Salinity Maximum Water (SMW), also called Subtropical Underwater (SUW). The SMW is formed in the

tropics-subtropics transition region, where the evaporation is stronger than precipitation. The subducted oxygen- and salinity-rich water progresses equatorward as a subsurface salinity maximum, while the water above is salinity-poor owing to the high precipitation in the tropics [Schott *et al.*, 1995]. Figure 3b shows surface water with salinities lower than 35.5 at 6.5°N, while values over 36 (gray shade) protrude from both north and south on the top of thermocline ( $\sigma_\theta = 24.5$ ).

[25] Underneath the TSW and SMW, the Atlantic Central Water is characterized by a linear  $\Theta$ -S relationship that extends up to the  $\sigma_\theta = 27.1$ , the Intermediary Layer [Stramma and Schott, 1999]. The South Atlantic Central

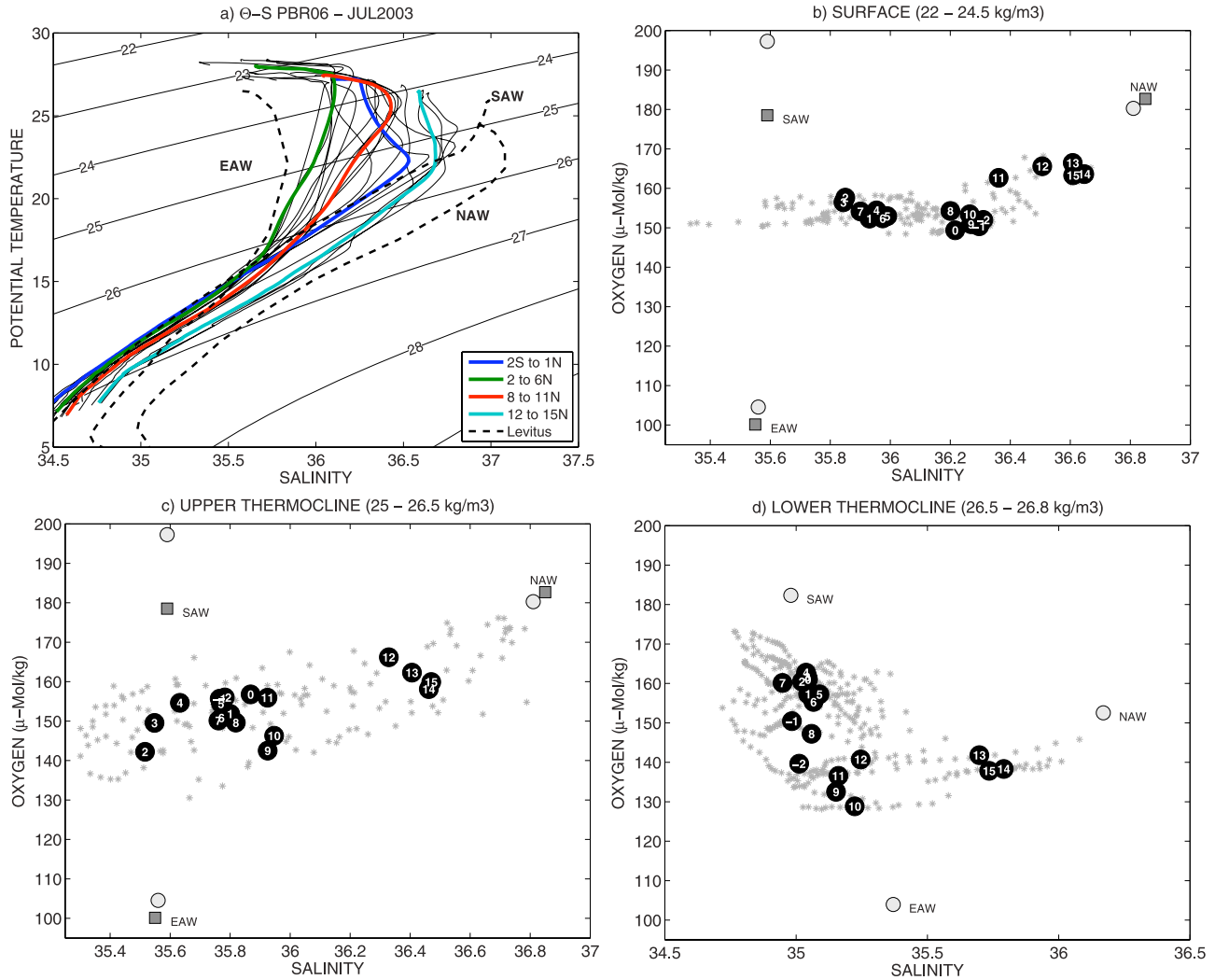


**Figure 4.** (a)  $\Theta$ -S diagram for JUL2003 cruise and distribution of salinity-oxygen values along 38°W in the (b) surface layer ( $\sigma_\theta$  from 22–24.5), (c) upper thermocline ( $\sigma_\theta$  from 25–26.5), and (d) lower thermocline ( $\sigma_\theta$  from 26.5–26.8). The gray stars display all oxygen-salinity values vertically distributed within the  $\sigma_\theta$  limits while the black circles are the mean value for each CTDO<sub>2</sub> profile. The white labels over the black circles are the latitudes of each CTDO<sub>2</sub> station and range from –2 to 15. The gray circles and squares are values of reference of South Atlantic Water (SAW), North Atlantic Water (NAW), and Eastern Atlantic Water (EAW) from Levitus and from *Wilson et al.* [1994], respectively.

Water (SACW) is fresher and warmer than the North Atlantic Central Water (NACW), and as shown by *Schott et al.* [1995], has high concentrations of dissolved oxygen. A separation between these two water masses is evident in the profiles of Figure 2 and in the contours of salinity (Figure 3b). In the  $\Theta$ -S diagram, the mean curve from 11 to 15°N is displaced far from the others profiles and is closer to the NAW reference curve. In the contour map, a salinity front is seen at 12°N. This feature extends zonally across the entire North Atlantic Ocean from the Caribbean Sea to the African coast, and is named the Cape Verde Frontal Zone (CVFZ) [Onken and Klein, 1991].

[26] Dissolved oxygen collected at each degree of latitude during JUL2003 allows to a more detailed water mass analysis along 38°W (Figure 4). Similarly to Figure 2, the  $\Theta$ -S diagram for JUL2003 is presented (Figure 4a). The meridional distribution of salinity-oxygen property is analyzed for three different layers of  $\sigma_\theta$ : the surface layer

(Figure 4b), the upper thermocline (Figure 4c), and the lower thermocline (Figure 4d). These three layers were chosen on the basis of Figure 3, which also displays the isopycnals of 25 and 26.5 used here as boundaries (gray lines). All salinity-oxygen values within each layer are represented in Figures 4c, 4d, and 4e by the gray stars while the mean value at each degree of latitude are represented by the black circles with latitudes labeled in white. Reference values of NAW, SAW, and EAW from Levitus (gray circles) and from *Wilson et al.* [1994] (squares) were added on the plots. The values at  $\sigma_\theta = 26.25$  were used in both Figures 4b and 4c since the  $\sigma_\theta = 24.5$  outcrops the surface equatorward the region of references. For the lower thermocline layer (Figure 4d), the reference values at  $\sigma_\theta = 26.5$  were used instead.

[27] In the surface layer (Figure 4b), the waters north of 11°N have oxygen concentration over 160  $\mu\text{Mol kg}^{-1}$  and salinity higher than 35.5. This water mass is a mixture of

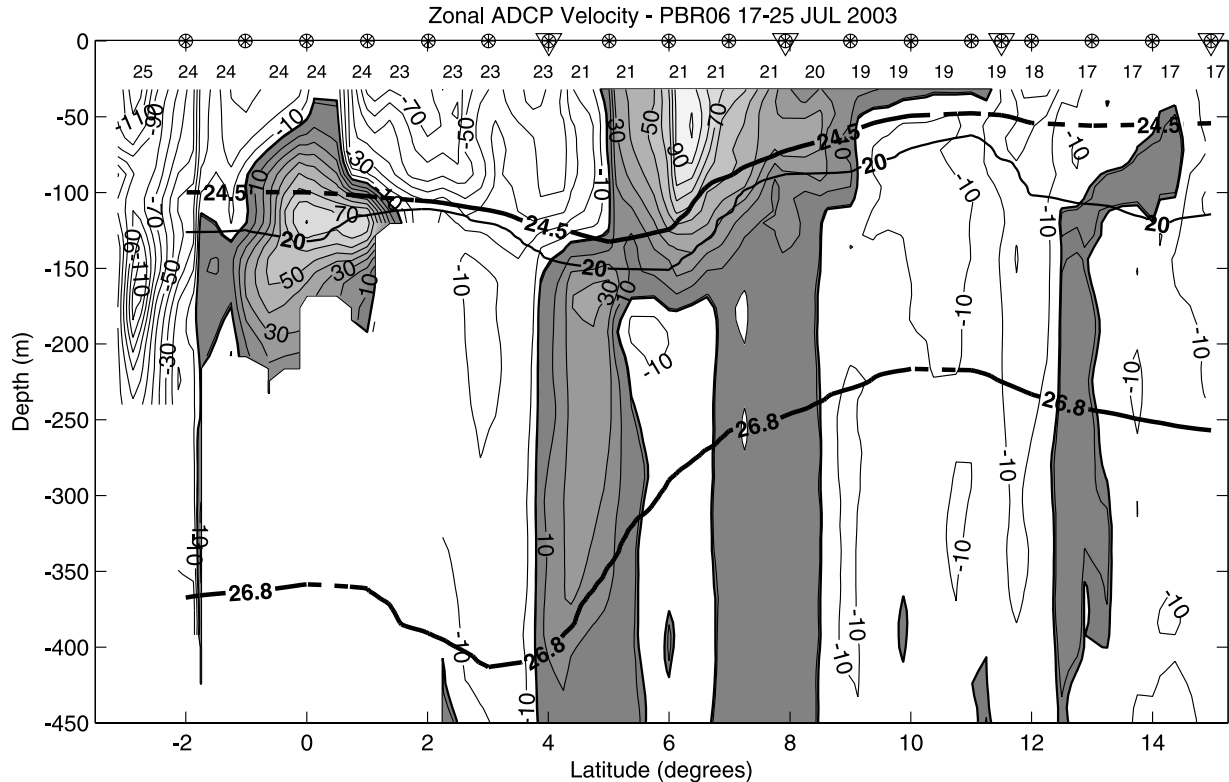


**Figure 5.** Zonal ADCP velocity along 38°W during JUL2003. Eastward velocities are the gray shades. The contour interval is  $10 \text{ cm s}^{-1}$ . The numbers in the top of the section are the days of July in which the ADCP collected the data. The circles are the CTDO<sub>2</sub> stations, and inverted triangles are ATLAS positions.

mostly NAW and EAW carried by the North Equatorial Current (NEC).

[28] The region southward of the equator (black circles labeled as 0, -1, and -2) has salinity-oxygen values similar to the region from 8 to 10°N (black circles labeled as 8, 9, and 10), however, it does not mean that the waters origin is the same. Figure 5 shows that at these southernmost latitudes is the cSEC, which is known by carrying a mix of EAW and surface high-salinity SAW. From 8°N to 10°N, the waters have a little higher-oxygen concentration due to a small part of NAW brought into the region by the nNECC.

[29] A strong vertical stratification with fresh low-oxygen waters near the surface over salty oxygen-rich waters on top of the thermocline (Figure 3) is found in the NECC region. Around 7°N, in the main NECC core, is a minimum of salinity that affects the mean value. This minimum is also represented in Figure 4b by the gray stars of salinity lower than 35.5. Excluding the very surface waters from the mean computation; i.e., using only  $\sigma_\theta$  of 24 to 24.5 (not shown), did not affect the mean value for all latitudes but 7°N.

[30] From 2 to 6°N, still in the surface layer, a mix of SAW and EAW associated with the nSEC and the southern edge of the NECC (Figure 5) is found. At the southern part of the nSEC, at latitudes 2 and 3°N, the oxygen concentration is higher than the northern part.

[31] In the upper thermocline (Figure 4c), the southern part of the section is a mix of SAW and EAW while north of 12°N is found high salinity and relative high-oxygen water (NAW + EAW). The low-oxygen core of  $140 \mu\text{-Mol kg}^{-1}$  at

2–3°N (EAW), seen in Figure 3c, is associated with the deeper nSEC, flowing between the EUC and the NEUC (Figure 5).

[32] In the lower thermocline layer ( $\sigma_\theta$  from 26.5 to 26.8; Figure 4d), only Levitus was used as reference (gray circles). In this layer, high oxygen and low-salinity water are restricted north of the equator up to 7°N, and are associated with the lower part of the EUC and the NEUC, carrying mostly SAW mixed with a small part of EAW. No NAW was found in the EUC during this cruise. This water is restricted north of 12°N. From 9 to 12°N, southward from the salinity front, the water is mostly EAW with a small part of SAW. A conclusive picture that shows if NAW is contributing to the water mass mixture south of 10°N will only be possible through Lagrangian tracers analysis.

### 3.2. Velocity Field

#### 3.2.1. JUL2003 Cruise

[33] Section 3.1 presented the distribution of water masses along 38°W during JUL2003. Here we will describe the velocity field shown by Figure 5.

[34] South of 2°S, the NBC has its maximum surface core of  $-120 \text{ cm s}^{-1}$  over 50-m depth. At 150-m depth is the NBUC with a maximum velocity of  $-110 \text{ cm s}^{-1}$ . From 2°S to the equator, the cSEC is an eastward surface flow of maximum velocity of  $-30 \text{ cm s}^{-1}$ . Between the equator and 5°N, the intensified nSEC has maximum velocity of  $-70 \text{ cm s}^{-1}$  at 2°N but a second maximum of  $-50 \text{ cm s}^{-1}$  exists south of 4°N. This strong westward flow extends as



deep as 450 m and has a maximum velocity of  $-10 \text{ cm s}^{-1}$  into the thermocline. At the equator, and surrounded by the intensified westward flows, the EUC has a maximum velocity of  $70 \text{ cm s}^{-1}$  at 125-m depth and between  $0^\circ\text{N}$  and  $1^\circ\text{N}$ . The structure of the EUC will be discussed ahead in conjunction with velocity maps of different seasons (section 3.2.2).

[35] The NEUC appears at  $4.5^\circ\text{N}$  with maximum eastward velocity of  $30 \text{ cm s}^{-1}$  at 175-m depth. In the  $\sigma_\theta$  level of 24.5 this current is connected with the lower part of the NECC, and extends downward the  $\sigma_\theta$  of 26.8, at 450-m depth. At  $6.5^\circ\text{N}$  and 70 m depth, the southern core of the North Equatorial Countercurrent (sNECC) reaches  $100 \text{ cm s}^{-1}$ . This current extends downward to 175-m depth, covering the surface layer and the upper part of the thermocline. The  $\sigma_\theta$  of 24.5 (and  $20^\circ\text{C}$ ) contours the opposing nSEC and NECC, with the deepest level centered in the region where the shear is strongest. At  $8^\circ\text{N}$ , the northern branch of the NECC (nNECC) reaches  $30 \text{ cm s}^{-1}$  at the same depth of the sNECC (70 m). From  $6.5^\circ\text{N}$  to  $8.5^\circ\text{N}$  and from the base of the NECC down to 500-m depth, there is an almost uniform vertical column of eastward flow weaker than  $10 \text{ cm s}^{-1}$ . Using model outputs, Urbano *et al.* [2006] describe this feature as the lower part of the nNECC. Details about the observed NECC double core will be discussed ahead in this text (section 3.2.3).

### 3.2.2. EUC

[36] Zonal velocity maps for the EUC region at  $38^\circ\text{W}$  are shown in Figure 6. On the left, the winter/spring cruises are FEB1999, MAR2000, and APR2001 (Figures 6a, 6b, and 6c), while in the right, the three summer cruises are JUL2003, JUL2004, and JUL2005 (Figures 6d, 6e, and 6f).

[37] During FEB1999 and MAR2000 (Figures 6a and 6b), although lacking measurements, it is possible to infer that the EUC is connected with the NEUC. During MAR2000, this connection is through a weak surface eastward flow at  $4^\circ\text{N}$ . On the other hand, during the summer cruises (Figures 6d, 6e, and 6f), the nSEC is stronger and deeper, and the NEUC is displaced northward and connected with the NECC only.

[38] From the near-surface velocity maps (Figure 7c), the EUC is a broad eastward flow from  $2^\circ\text{S}$  to  $3^\circ\text{N}$  from January to June, and again in August/September of each year. The three boreal summer cruises presented in Figure 6 have westward surface velocity over the EUC, before the second EUC maximum in the seasonal cycle. During 2000, a northward propagation of the surface EUC of  $20\text{--}40 \text{ cm s}^{-1}$  is seen from  $1^\circ\text{N}$  in March/April up to  $4^\circ\text{N}$  in May/June, before the SEC intensification. The variability of the near-surface EUC at  $38^\circ\text{W}$  will be presented in section 3.3.

[39] The  $1/4$ -degree resolution maps of Figure 6 suggest that during winter/spring the EUC core has two subsurface maxima at  $38^\circ\text{W}$ , which are most evident during APR2001 (Figure 6c). Both maxima have  $100 \text{ cm s}^{-1}$ , with one at  $1^\circ\text{N}$  and 100-m depth and the second at  $1.5^\circ\text{N}$ , 70-m depth. The days in which the velocity was measured by the ADCP are displayed on top of each map. Figures 6c and 6f show that the EUC was observed from April 10 to April 11 for the cruise APR2001, and during July 14 for the cruise JUL2005. This current was measured within a 24-h interval, which usually avoids meandering (aliasing) effects. During

the July cruises, the EUC core has only one maximum just below 100-m depth and centered at  $0.5\text{--}1^\circ\text{N}$ .

### 3.2.3. NECC

[40] Zonal velocity maps for the NECC region at  $38^\circ\text{W}$  are shown in Figure 8. The winter/spring cruises (February, March, and April) are on the left, while the July cruises (boreal summer) are on the right. These six vertical sections do not form a complete seasonal cycle, but together with the time series of near-surface velocity (Figures 7a and 7b), shed light on the meridional displacement of the NECC two-core structure, mainly in the poorly measured region northward of  $7.5^\circ\text{N}$ .

[41] During FEB1999 (Figure 8a), the sNECC extends from  $5.5^\circ\text{N}$  to around  $8^\circ\text{N}$  and reaches  $30 \text{ cm s}^{-1}$  at  $6.5^\circ\text{N}$ . Dominating the upper 250 m from  $9$  to  $14.5^\circ\text{N}$ , there is a broad eastward velocity flow composed of two regions of  $20 \text{ cm s}^{-1}$  in the surface layer (above  $\sigma_\theta = 24.5$ ): one at  $10.5^\circ\text{N}$  and other at  $13^\circ\text{N}$ ; they are separated by a weak eastward flow. Underneath the  $\sigma_\theta$  of 24.5, a column of eastward flow of  $10 \text{ cm s}^{-1}$  is associated with each surface nNECC eastward maximum.

[42] From the near-surface velocity (Figure 7a), the NECC bifurcates at  $6^\circ\text{N}$  just before the sNECC intensification in August/September. The two eastward flows (sNECC and nNECC), which are separated by a westward flow, start to migrate northward following the ITCZ displacement. During FEB1999, the nNECC reaches its northernmost position and starts the southward migration. At the same time, the sNECC becomes weaker up to April/March. The sNECC reverses (at least near the surface) in the region from  $4$  to  $10^\circ\text{N}$ , but the nNECC remains in the region north of  $10^\circ\text{N}$ . A new eastward intensification starts at  $2$  to  $4^\circ\text{N}$  (Figure 7a). In May/June, the sNECC at  $6$  to  $8^\circ\text{N}$  intensifies again and starts the northward excursion. After the bifurcation, waters from the nNECC meet with the nNECC waters from the previous year that are migrating southward. At this point, the seasonal cycle is closed and repeats at each year. The variability of this near-surface time series will be presented in section 3.3.

[43] The same scenario of FEB1999 occurs during MAR2000. From Figure 7a, the nNECC presents a complex structure before starting the southward migration. In these two cruises, the nNECC of the previous year added to waters that enter the region from north (from the NEC) all year long. The APR2001 cruise registered the minimal eastward flow across  $38^\circ\text{W}$  (Figure 8c) during this season, when the ITCZ has its southernmost position in the annual cycle.

[44] During JUL2003 and JUL2004 (Figures 8d and 8e), the two NECC cores are closer. From the subsurface velocity maps, the nNECC is associated with a deeper eastward flow from  $7^\circ\text{N}$  to  $8.5^\circ\text{N}$  at Figure 8d, and from  $5$  to  $7^\circ\text{N}$  at Figure 8e. From Figure 7a, it is possible to see that the nNECC is connected to the sNECC, occupying its southernmost position just before starting to migrate northward during August through April/March.

## 3.3. Variability at $38^\circ\text{W}$

[45] As seen in the section 3.2.3, the NECC exhibits a very strong seasonal character driven by the meridional migration of the Atlantic ITCZ throughout the year. To a first approximation, the transport of the NECC is in



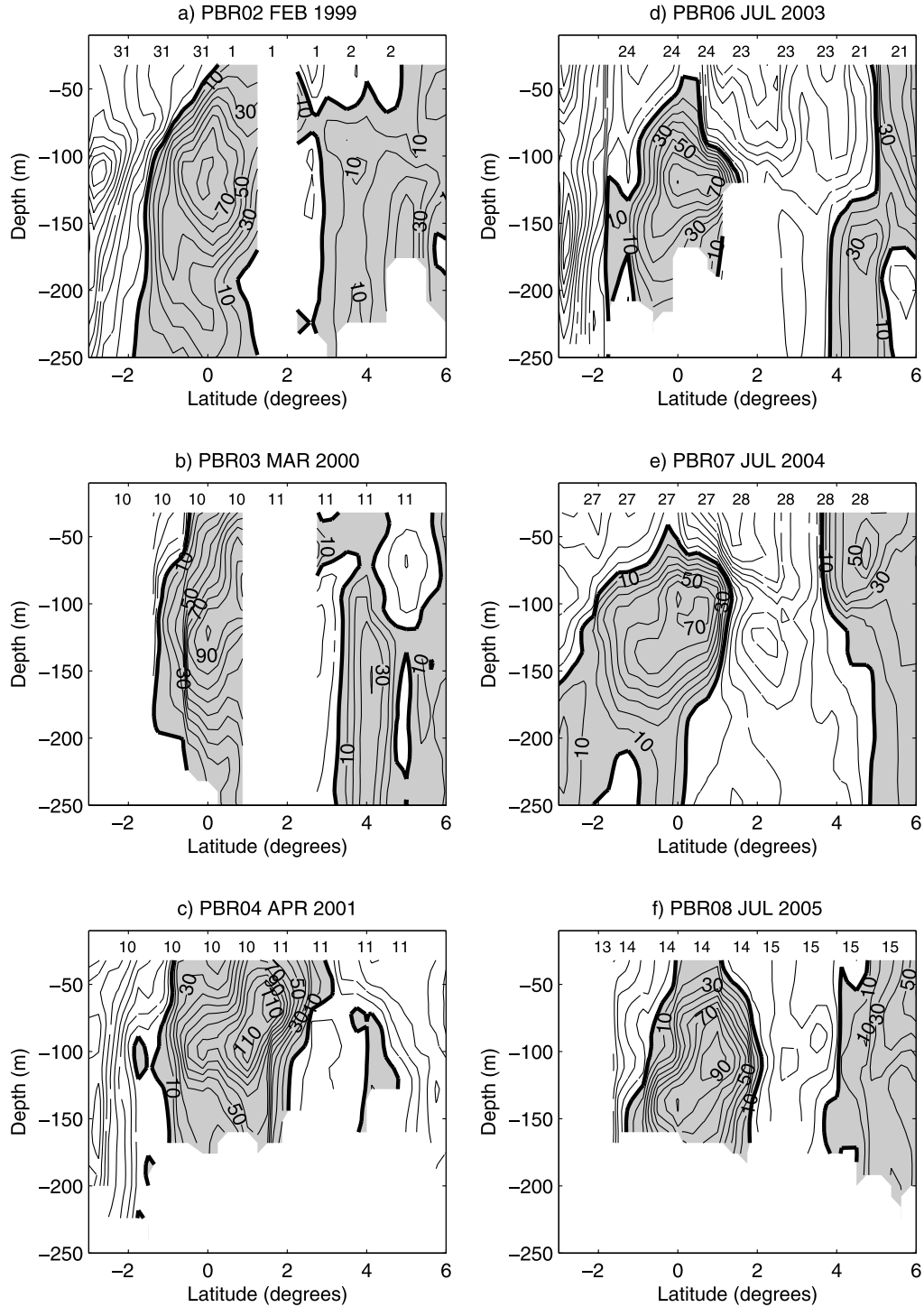


**Figure 6.** Zonal ADCP velocity in the EUC region at 38°W collected during winter/spring: (a) FEB1999, (b) MAR2000, and (c) APR2001; and during summer: (d) JUL2003, (e) JUL2004, and (f) JUL2005. Shaded areas are eastward velocities with contours at each 10 cm s<sup>-1</sup>. The days in which the ADCP collected the data are displayed on top of each map.

Sverdrup balance, following the wind stress curl with a lag of 1–3 months due to the timescale of Rossby waves propagation across the Atlantic from the coast of Africa [Urbano *et al.*, 2006; Fonseca *et al.*, 2004]. In this section we will show that the seasonality of the wind stress curl in the tropical Atlantic can explain the presence of the observed

two-core structure of the NECC, as well as the northward migration of the system starting after May.

[46] To investigate the seasonal cycle of the NECC we used the near-surface velocity data for the period between 07 January 1998 and 20 September 2006 for the 38°W section between 4°S and 15°N. The zonal geostrophic

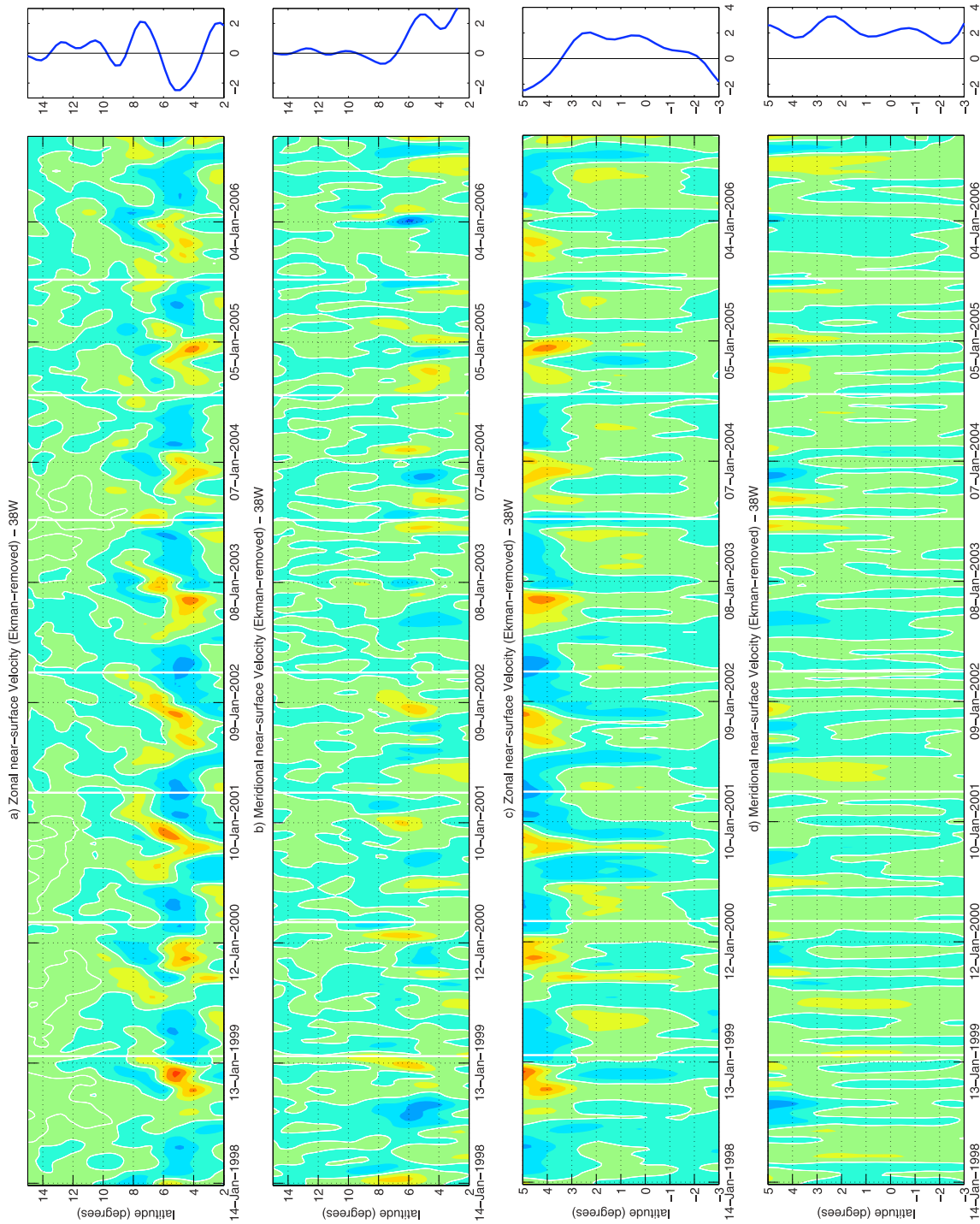


**Figure 7.** Near-surface Ekman-removed zonal (a and c) and meridional (b and d) velocity component along 38°W for the NECC and EUC region. The original  $1/3^\circ$  by  $7\text{-d}$  resolution was smoothed using a running mean filter of 5 points. Contour intervals are  $20\text{ cm s}^{-1}$  with red eastward (northward) and blue westward (southward) flow. White lines show the time of each annual PIRATA ADCP cruise coincides with the data set. The time-mean of each velocity map is on the right.

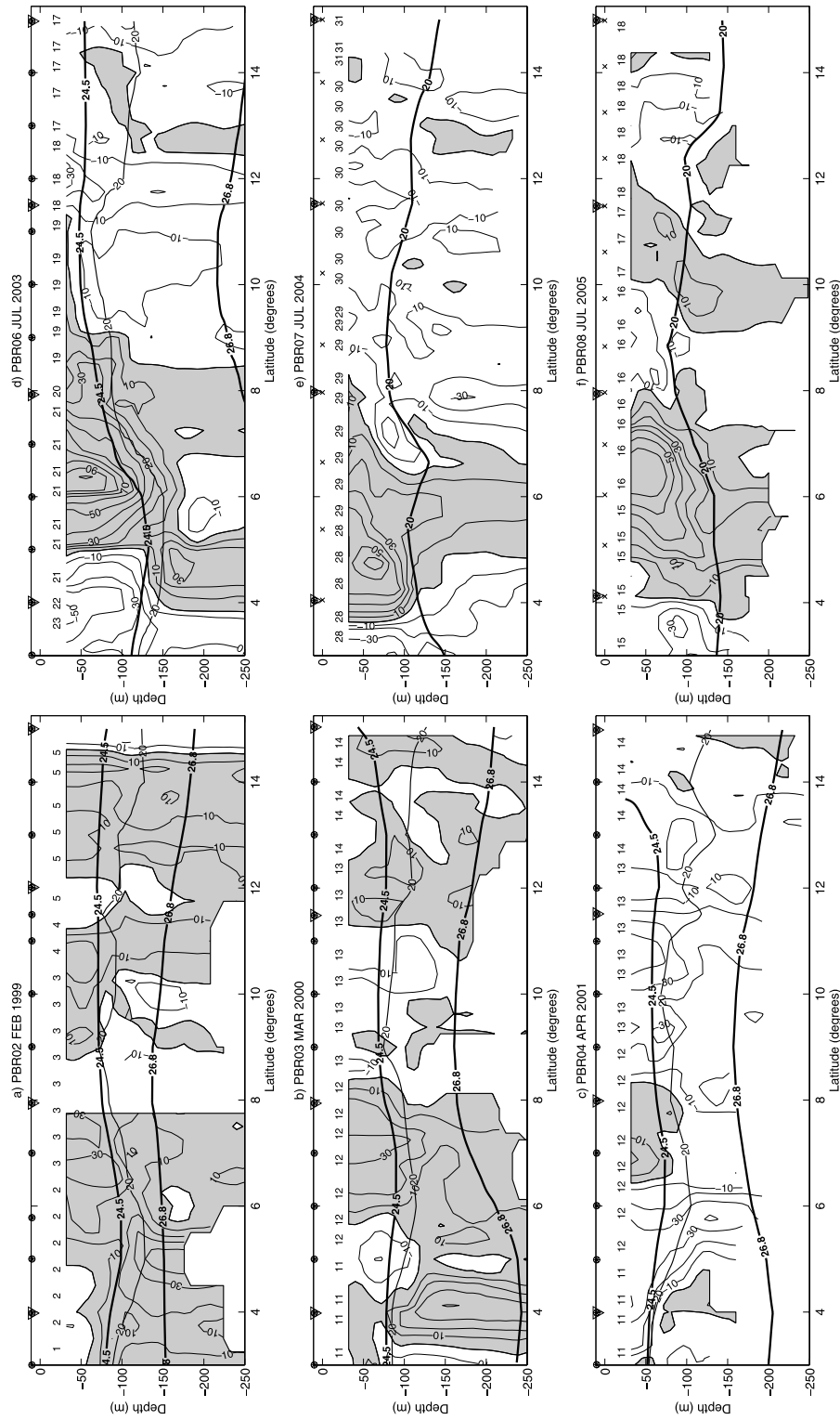


**Figure 8.** Zonal ADCP velocity in the NECC region at 38°W collected during winter/spring: (a) FEB1999, (b) MAR2000, and (c) APR2001; and during summer: (d) JUL2003, (e) JUL2004, and (f) JUL2005. Shaded areas are eastward velocities with contours at each 10 cm s<sup>-1</sup>. The days in which the ADCP collected the data are displayed on the top of each map. Superimposed are the  $\sigma_\theta$  layers of 24.5 and 26.8 (thick lines) and temperature of 20°C (thin lines). Circles are CTD stations, and triangles are ATLAS moorings locations. Figures 8e and 8f display XBT temperatures only with the stations marked by “x”.



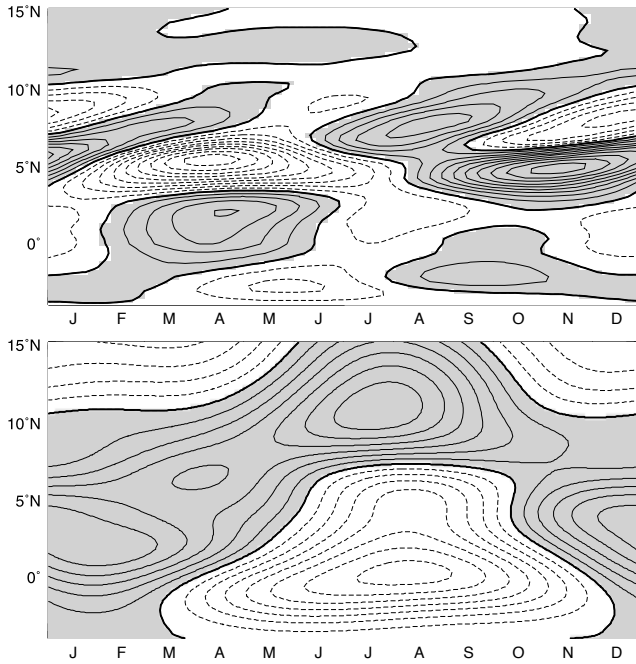


**Figure 9.** Seasonal cycle (annual and semiannual harmonics) at 38°W of (top) long-term anomalies of geostrophic zonal near-surface velocity; contour interval (CI) is  $5 \text{ cm s}^{-1}$ . (bottom) Wind stress curl from Quikscat; CI =  $1 \text{e} - 8 \text{ Pa m}^{-1}$ . Positive values are gray shaded, and negative values are dashed.

velocity field was decomposed into its annual and semiannual harmonics using a least squares fit [Podestà *et al.*, 1991]. The results, displayed in Figure 9 (top), reveal the annual cycle of the zonal current system in the tropical Atlantic, while Figure 9 (bottom) shows the seasonal cycle of the wind stress curl, obtained from wind products from the Quikscat scatterometer.

[47] The 4°S–4°N band of the section at 38°W in Figure 9 (top) shows the semiannual surfacing of the EUC. During late boreal summer the EUC appears predominantly on the Northern Hemisphere, showing a meridionally elongated structure extending from the equator up to 2°N. The EUC disappears from the surface during June and July, reappearing shifted toward the Southern Hemisphere during late boreal winter and early fall, albeit with a lower magnitude. The surface core of the EUC weakens again from December to February, when it migrates back to the Northern Hemisphere and reintensifies, closing its seasonal cycle. This semiannual pattern is consistent with numerical modeling results from Arhan *et al.* [2006], showing different regimes during summer–autumn and winter–spring for the EUC.

[48] North of the EUC, flowing westward, lies the nSEC, stronger during March–April–May and located at 5°N. At the beginning of June the nSEC is displaced southward by an intensified NECC that appears at 6°N with the northward migration of the ITCZ, indicated by the equatorward zero curl line in Figure 9 (bottom). Early in September the NECC bifurcates, giving rise to the sNECC and the nNECC, separated by a westward flow. The sNECC reaches a maximum velocity of  $45 \text{ cm s}^{-1}$  at 5°N from October to December, while the nNECC peaks at 7°N during August–September at  $20 \text{ cm s}^{-1}$ . The formation of the two cores can be seen in Figure 10a, showing the zonal velocity at the section averaged for the months of August–September–October (ASO) in a thick line. The double-core structure of the NECC is driven by the ITCZ with a time lag of 3 months, as revealed by the averaged wind stress curl for May–June–July (MJJ), depicted by the gray filled curve.

[49] Throughout the year the two NECC cores follow the displacement of a second line of zero wind stress curl toward north, gradually weakening by the end of the year as the ITCZ starts its southward migration. This final stage of the sNECC/nNECC can be seen in Figure 10b, showing the averaged zonal velocity during May–April–March (MAM), when both currents are located at 7°N and 12°N,

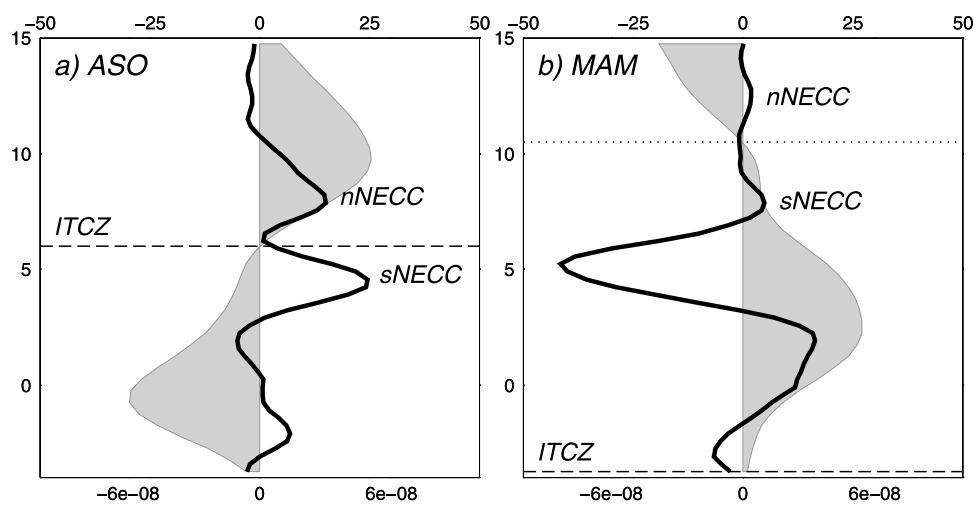


**Figure 10.** Time-averaged zonal velocity (thick black line,  $\text{cm s}^{-1}$ , scale at top) and wind stress curl (filled gray line,  $\text{Pa m}^{-1}$ , scale at bottom) lagged by 3 months at 38°W. (a) August–September–October (zonal velocity) and May–June–July (wind stress curl); (b) March–April–May (zonal velocity) and December–January–February (wind stress curl). The ITCZ position (dashed line) is derived from the zero wind stress curl closest to the equator. The dotted line shows a secondary zero curl wind stress.

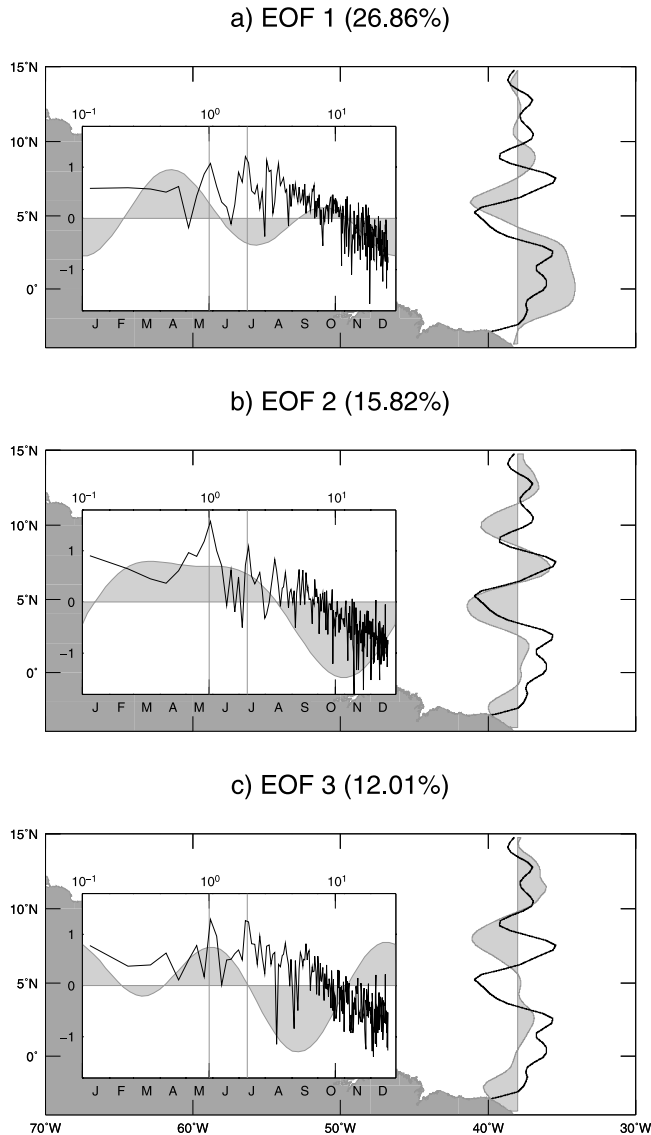


**Figure 11.** EOFs of the long-term anomalies of geostrophic zonal near-surface velocity, with explained variance in parenthesis. The filled gray line in the 38°W section shows the EOF loading, while the thick black line shows the mean field. The subplots show the spectra and annual plus semiannual harmonics of the corresponding normalized expansion coefficients.

respectively. During this period the ITCZ occupies its southernmost position, and the location of two cores of the NECC coincide with the zero curl line at 10.5°N. Later in May, when both cores have reached their northernmost position, the NECC dies just as another cycle starts. While the Hövmøller diagram in Figure 7a shows recurring connections between two nNECC cores from consecutive years, this is not seen here on the seasonal cycle, suggesting an intermittent pattern.

[50] In order to quantify the dominant modes of seasonal variability in the tropical Atlantic, we conducted an empirical orthogonal function (EOF) analysis of the SVP time series using the zonal geostrophic anomalies at 38°W. The anomalies were constructed by removing the long-term

average geostrophic velocity at each grid point, and were further normalized by the local standard deviation to give similar weight to different latitudes. The results, presented in Figure 11, show the first three EOFs (filled gray curve) normalized by one standard deviation and plotted against the mean velocity field at 38°W (thick black line). On each graphic in Figure 11, a subplot shows the spectrum and the seasonal cycle of the corresponding expansion coefficients. The first three modes explain up to 55% of the total variance in the zonal current system, suggesting that a considerable fraction of the remaining variance in the region is caused by turbulent flow.

[51] The first mode shows a predominantly semiannual and annual character that captures up to 27% of the zonal variability at 38°W. This leading mode has a strong loading between 2°S and 4°N, corresponding to the seasonal cycle of the EUC during March–April–May and late boreal fall, when the current is intensified and reaches the surface. The EOF confirms that the EUC has a stronger amplitude during the first half of the year, as seen on the seasonal velocity field (Figure 9). North of the EUC there is also a significant amplitude in this mode, depicting the currents with alternating directions present at the 6°N latitude throughout the year: sNECC (January–February), nSEC (March–April–May), nNECC (June–September) and finally the counterflux between the nNECC and the sNECC (October–December).

[52] The second EOF, explaining 16% of the variance, corresponds to an annual mode of variability outside the EUC band. This mode represents the alternation of the nSEC at 4–5°N for the sNECC after August, when the effect of the northward migration of the ITCZ starts to be expressed on the zonal current system. The northern band of the mode loading, between 6°N and 12°N, depicts the migration of the sNECC and nNECC cores to the northern part of the basin, when the seasonal cycle of the expansion coefficients reverse sign. A similar pattern suggesting a propagative mode is also found on the third EOF (12%) between 6°N and 14°N. The combination of these two modes captures the cycle of annual migration of the NECC cores in the tropical Atlantic.

#### 4. Discussion

[53] From the water mass analysis presented in section 3.1 it was shown that, along 38°W, waters from the North Atlantic (NAW) occupy the region north of 11°N, while south of it there is a mixed water mass named by Schott *et al.* [1995] Equatorial Water. This water mass has a contribution from the South Atlantic through the NBC retroflexion, from the Eastern Atlantic through the NEC and SEC, and also from the North Atlantic. Water mass analysis also shows that the NECC carries mixed water composed by SAW, EAW and NAW. Wilson *et al.* [1994], Schott *et al.* [1998], and Boulès *et al.* [1999a] had already shown that the NECC is fed by waters from South and North Atlantic oceans from the NBC retroflexion and NEC recirculation, respectively. However, the water mass analysis did not explain how the NAW entered the 38°W section. Lagrangian tracers and high-resolution modeling need to be used for better understanding this issue.

[54] Relatively high-salinity waters in the EUC shows that waters from the subtropical subduction region are

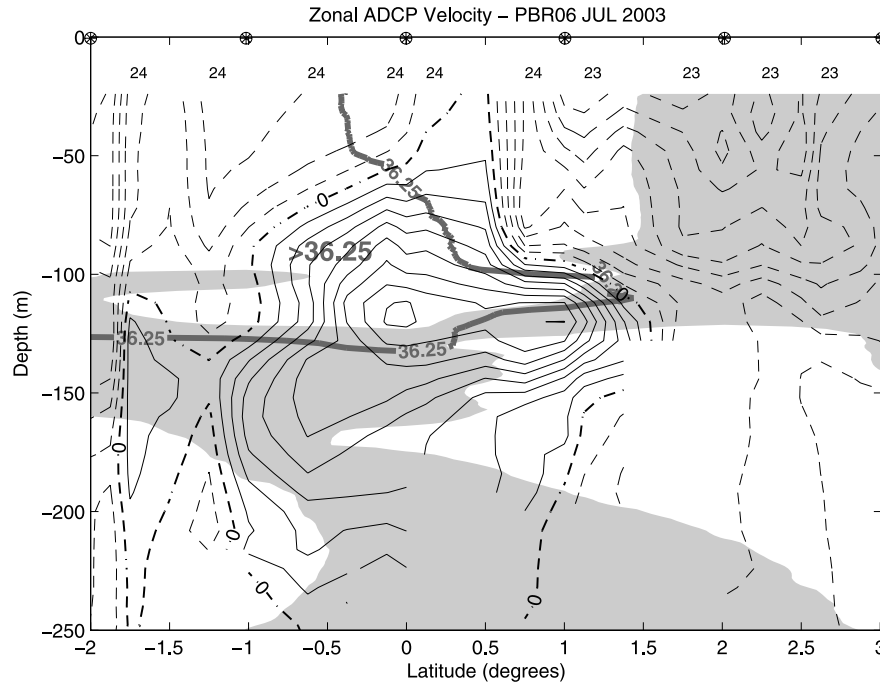


**Figure 12.** Zonal velocity in the EUC during JUL2003. Salinity higher than 36.25 is contoured by the thick gray line. The region of dissolved oxygen higher than  $155 \mu\text{-Mol kg}^{-1}$  is shaded (gray). Circles are the CTD stations, and numbers are days.

carried by this current. However, from salinity alone it is not possible to verify whether these waters are from the subtropical North or South Atlantic regions and dissolved oxygen became an important parameter in the water mass analysis. North Atlantic subducted water is characterized by high concentration of dissolved oxygen and high salinity. Figure 12 shows that the relative high dissolved oxygen is not associated with high-salinity waters during JUL2003. The high-oxygen concentration is associated with the deeper EUC and with relative low-salinity waters. Therefore, the JUL2003 analysis agrees with the previous observational results presented by *Bourlès et al.* [1999a] and *Schott et al.* [1995], that show no North Atlantic water being carried by the EUC.

[55] It was shown by the observational work of *Goes et al.* [2005] that the single EUC core at  $41^\circ\text{W}$  separates into the NEUC and EUC by  $35^\circ\text{W}$  during February 2002. The EUC at  $38^\circ\text{W}$ , i.e., between the two longitudes investigated by *Goes et al.* [2005], was described here (section 3.2.2). The single EUC core at  $38^\circ\text{W}$  is composed by two maxima that are most evident during APR2001. Because of the lack of measurements in the EUC around  $2^\circ\text{N}$  during FEB1999 it was not possible to infer a second EUC core at this longitude. The data described here suggest that the EUC bifurcation, if it occurs by  $35^\circ\text{W}$  as described by *Goes et al.* [2005], occurs eastward of  $38^\circ\text{W}$ .

[56] The two maxima in the EUC core are frequently observed, but as discussed by *Bourlès et al.* [1999a], they could be generated by the strong EUC meandering activity. A double sampling of the current can occur because of the ADCP profiles being not simultaneous along the section. Here, the EUC region was measured during a period smaller than 24 h, as shown by Figure 6, which avoids meandering effects on the data set. Therefore, the two maxima described

here in the EUC core are not due to observational aliasing and should have a dynamical forcing. Preliminary high-resolution ( $1/8^\circ$ -degree) results from a daily wind forced Ocean General Circulation Model (OGCM) are able to reproduce the two features in the EUC core (not shown), with the two maxima approaching and receding each other on monthly timescales in association with the SEC intensification just above the EUC. These results agree with the spectral analysis presented in Figure 11a, which shows peaks of energy around 30 d, and suggest that the two maxima could be the result of the superposition of Tropical Instability Waves (TIW, see *Jochum et al.* [2004]) over the EUC. However, no TIW signal was found in the geostrophic velocity during March/April/May, when the two maxima in the EUC core were more evident (Figure 6c). During this period, the computed 30-d Eddy kinetic energy (EKE) is minimum for every year but 2002. On the other hand, the influence of TIWs at  $38^\circ\text{W}$  cannot be ruled out. Observing these waves with an altimeter is difficult given the short timescales and length scales of TIWs [*Jochum et al.*, 2004]. A more thorough investigation using numerical modeling is necessary in order to understand these processes and verify if these features can evolve to a bifurcation of the EUC.

[57] Figure 9 includes the equatorial region ( $2^\circ\text{N}$  up to  $4^\circ\text{S}$ ) and allowed the investigation of the seasonal cycle of the surface flow in the EUC region. During FEB1999 (Figure 6), despite the lack of profiles, the nearby velocities suggest a subsurface flow near  $2^\circ\text{N}$ . An eastward near-surface flow with velocities of up to  $40 \text{ cm s}^{-1}$  above the EUC has already been observed, as discussed by *Bourlès et al.* [1999b]. The authors mention that a possible explanation for this flow is the near-equatorial location of the ITCZ that leads to a relaxation of the wind forcing and an eastward pressure gradient. However, an eastward flow above the



EUC was observed around 2°S in September 1995 and during two October cruises described by *Schott et al.* [1998], time in which the ITCZ has its northernmost position. Here, Figure 9 shows that the EUC reaches the surface at 2°N in April, and again at 2°S in September/October. The first maximum is associated with the southward ITCZ position while the second maximum is associated with a strong gradient in the wind stress curl field. The EOF analysis revealed that the EUC variability is dominant on the tropical Atlantic, confirming its semiannual character in agreement with the observations and with the modeling results of *Arhan et al.* [2006].

[58] From the combination of high-resolution subsurface ADCP velocity and near-surface Ekman-removed velocity field along 38°W, the NECC two-core structure and seasonal cycle was described. Motivated by model results, *Urbano et al.* [2006] showed that the NECC is composed by two cores and lies between 3°N and 13°N. In this work, it was shown that the nNECC is an eastward flow lying between 9°N and 15°N that migrates northward and southward following the wind field seasonal fluctuation throughout the whole year. The observational data shows that during FEB1999 and MAR2000 the nNECC was composed of two eastward flows separated by a westward flow, in agreement with the nNECC two branches observed by *Stramma et al.* [2005a] in the eastern tropical Atlantic. The two branches were also measured in the near-surface velocity data (Figure 7), and can be explained by the Sverdrup transport driven by the wind field.

[59] It was shown here through the annual cycle of the zonal current system (Figure 9 (top)) that, including the region from 9 to 15°N, no NECC reversal was found. The NECC intensifies at 6°N in June/July and bifurcates in August/September. The northern branch migrates northward up to 13–14°N along the year, while the southern branch centered at 5°N reaches the maximum NECC velocities in September. Instead of reversal, this sNECC starts to migrate northward in January–February, displacing from 5°N to 10°N, while the nNECC intensifies at 5°N during March/April/May. This migration is confirmed by the EOF analysis, appearing as a combination of the second and third modes. An important feature of the nNECC cycle is that occasionally waters from the current at the end of its lifecycle will feed a newly formed nNECC that is migrating to the north, persisting on the basin from one year to the next. This phenomenon can be seen during the years 1998, 1999, 2000, 2003 and 2005 (Figure 7a), where a year-old nNECC fed with waters from the Northern Hemisphere drifts southward and connects to the active nNECC core. These events suggest the existence of a memory of the zonal current system in tropical Atlantic, with possible implications for predictability and climate feedbacks.

[60] As discussed by *Fonseca et al.* [2004], the location of the NECC closely follows the annual migration of the ITCZ except during boreal winter, when it exhibits a secondary northward maximum. During this period the ITCZ is still approaching its southernmost position, unable to force the second eastward flow observed on the NECC. This fact raises the following question: what is driving the northward NECC maximum?

[61] The analysis of the wind stress curl field (Figures 9 and 10) sheds light on this question. For ASO (Figure 10a),

the ITCZ reaches its northernmost location and the two NECC cores are developed as discussed by *Urbano et al.* [2006], from a broad ITCZ. However, during MAM, it is a secondary zero line wind stress curl (Figure 10b, dotted line) that displaces southward to accelerate the eastward flow associated with the NECC, consistent with the 3 months time lag presented by *Fonseca et al.* [2004]. Therefore, the results presented here complete both previous works of *Urbano et al.* [2006] and *Fonseca et al.* [2004].

## 5. Summary and Conclusion

[62] Additional information about the upper ocean circulation was provided using hydrographic observations and direct velocity measurements along 38°W from 1998 to 2006. The ADCP velocity data described here are novel observations, since the meridional sections extended up to 15°N while the previous direct velocity data northernmost latitudes reached only up to 7.5°N. Even though supplying high resolution in the vertical, the seven ADCP sections do not fill the seasonal cycle of the zonal current system. Combined with the high-resolution near-surface velocity data a realistic picture of the structure and seasonal cycle of the EUC and NECC could be presented.

[63] One of the most important results of this work is the direct measurement of the NECC northern branch (nNECC). In a recent paper, *Urbano et al.* [2006] rediscovered the NECC second core, but the strongest observational evidence of this feature was only found, at that time, in ship drift and surface drifter data. Until the PIRATA ADCP data, the NECC second core had never been observed directly in the western tropical Atlantic. *Lumpkin and Garzoli* [2005] used direct velocity near-surface data derived from the drifters alone to describe the surface circulation in the tropical Atlantic, but the velocity maps with 1° of meridional resolution averaged by 5° zonally masked out the nNECC features.

[64] Using the ADCP data combined with the high-resolution SVP (1/3° each 7 d) allowed a more detailed description of the NECC two-core structure and variability. An important feature of the nNECC annual cycle is that waters from the current at the end of its lifecycle will feed a newly formed nNECC that is migrating to the north, persisting on the basin from one year to the next.

[65] However, the most important result was found from the analysis of the wind stress curl from QuikSCAT satellite and the mean near-surface velocity map. What drives both the sNECC and nNECC is the convergence and divergence of the wind stress curl, which has two lines of zero curl: the ITCZ and a secondary northward zero line.

[66] The direct velocity data described here were invaluable to complete the investigations using the high-resolution time series from the ATLAS systems. However, subsurface measurements during the fall season are still missing. The observational discussions presented in this note are currently being subject of high-resolution ocean modeling at CPTEC/INPE, and shall contribute to enlarge the picture inferred from the observational evidence presented here.

[67] **Acknowledgments.** The authors are thankful to Rick Lumpkin from AOML/NOAA, who did the synthesis of and kindly provided the near-surface geostrophic data for the tropical Atlantic, and to the Brazilian Navy for the observational data set. The authors are also thankful to Julia

Hummon from University of Hawaii for the support with the ADCP data processing and to Markus Jochum for insightful discussions. The first author was supported by CNPq grant 154158/2006-2.

## References

- Arhan, M., H. Mercier, B. Bourlès, and Y. Gouriou (1998), Hydrographic sections across the Atlantic at 7°30N and 4°30S, *Deep Sea Res., Part I*, 45, 829–872.
- Arhan, M., A. M. Treguier, B. Bourlès, and S. Michel (2006), Diagnosing the annual cycle of the Equatorial Undercurrent in the Atlantic Ocean from a general circulation model, *J. Phys. Oceanogr.*, 36, 1502–1522.
- Bourlès, B., Y. Gouriou, and R. Chuchla (1999a), On the circulation in the upper layer of the western equatorial Atlantic, *J. Geophys. Res.*, 104(C9), 21,151–21,170.
- Bourlès, B., R. L. Molinari, E. Johns, W. D. Wilson, and K. D. Leaman (1999b), Upper layer currents in the western tropical North Atlantic (1989–1991), *J. Phys. Oceanogr.*, 104(C1), 1361–1375.
- Bourlès, B., M. D'Orgeville, G. Eldin, Y. Gouriou, R. Chuchla, Y. DuPenhoat, and S. Arnault (2002), On the evolution of the thermocline and subthermocline eastward currents in the equatorial Atlantic, *Geophys. Res. Lett.*, 29(16), 1785, doi:10.1029/2002GL015098.
- Csanady, G. T. (1987), What controls the rate of equatorial warm water mass formation?, *J. Mar. Res.*, 45, 513–532.
- DHN (2005), Relatório de fim de comissão: Operação “PIRATA BR VI”, technical report, Marinha do Brasil, Departamento de Hidrografia e Navegação, Navio Oceanográfico ANTARES, Niterói, Rio de Janeiro, Brazil.
- Diden, N., and F. Schott (1993), Eddies in the North Brazil Current retroflection region observed by Geosat altimetry, *J. Geophys. Res.*, 98, 20,121–20,131.
- Firing, E., J. Ranada, and P. Caldwell (1995), *Processing ADCP Data with the CODAS Software System Version 3.1.*, Joint Inst. for Mar. and Atmos. Res./NODC, Univ. of Hawaii at Manoa, Honolulu.
- Fonseca, C. A., G. J. Goni, W. E. Johns, and E. J. D. Campos (2004), Investigation of the North Brazil Current retroflection and North Equatorial Countercurrent variability, *Geophys. Res. Lett.*, 31, L21304, doi:10.1029/2004GL020054.
- Garzoli, S. L. (1992), The Atlantic North Equatorial Countercurrent: Models and observations, *J. Geophys. Res.*, 97, 17,931–17,946.
- Garzoli, S., and P. Richardson (1989), Low-frequency meandering of the Atlantic North Equatorial Countercurrent, *J. Geophys. Res.*, 94, 2079–2090.
- Goes, M., R. Molinari, I. C. A. Silveira, and I. Wainer (2005), Retroflections of the North Brazil Current during February 2002, *Deep Sea Res., Part I*, 52, 647–667, doi:10.1016/j.dsr.2004.10.010.
- Grasshoff, K., M. Ehrhardt, and K. Kremling (1983), *Methods of Seawater Analysis*, 2nd ed., Verlag Chemie, New York.
- Hansen, V. D., and P.-M. Poulain (1996), Quality control and interpolations of WOCE-TOGA drifter data, *J. Atmos. Oceanic Technol.*, 13, 900–909.
- Inui, T., A. Lazar, P. Malanotte-Rizzoli, and A. Busalacchi (2002), Wind stress effects on subsurface pathways from the subtropical to tropical Atlantic, *J. Phys. Oceanogr.*, 32, 2257–2276.
- Jochum, M., and P. Malanotte-Rizzoli (2003), On the generation of North Brazil Current rings, *J. Mar. Res.*, 61(2), 147–162.
- Jochum, M., P. Malanotte-Rizzoli, and A. Busalacchi (2004), Tropical instability waves in the Atlantic Ocean, *Ocean Modell.*, 7, 145–163.
- Joyce, T. M. (1989), On the in-situ calibration of shipboard ADCPs, *J. Atmos. Oceanic Technol.*, 6, 169–172.
- Lazar, A., T. Inui, P. Malanotte-Rizzoli, A. Busalacchi, L. Wang, and R. Murtugudde (2002), Seasonality of the ventilation of the tropical Atlantic thermocline in an ocean general circulation model, *J. Geophys. Res.*, 107(C8), 3104, doi:10.1029/2000JC000667.
- Levitus, S., R. Burgett, and T. P. Boyer (1994), *World Ocean Atlas 1994*, vol. 3, *Salinity*, NOAA ATLAS NESDIS 3, 111 pp., U.S. Govt. Print. Off., Washington, D. C.
- Lumpkin, R., and S. Garzoli (2005), Near-surface Circulation in the tropical Atlantic Ocean, *Deep Sea Res., Part I*, 52(3), 495–518.
- Malanotte-Rizzoli, P., K. Hedstrom, H. Arango, and D. Haidvogel (2000), Water mass pathways between the subtropical and tropical ocean in a climatological simulation of the North Atlantic ocean circulation, *Dyn. Atmos. Oceans*, 32, 331–371.
- Metcalf, W. G., and M. C. Stalcup (1967), Origin of the Atlantic Equatorial Undercurrent, *J. Geophys. Res.*, 72, 4959–4975.
- Niiler, P. P., N. A. Maximenko, G. G. Panteliev, T. Yamagata, and D. B. Olson (2003), Near-surface dynamical structure of the Kuroshio Extension, *J. Geophys. Res.*, 108(C6), 3193, doi:10.1029/2002JC001461.
- Onken, R., and B. Klein (1991), A model of baroclinic instability and waves between ventilated gyre and the shadow zone of the North Atlantic Ocean, *J. Phys. Oceanogr.*, 21, 53–67.
- Philander, S. G. H., and R. C. Pacanowski (1986), A model of the seasonal cycle in the tropical Atlantic Ocean, *J. Geophys. Res.*, 91, 14,192–14,206.
- Podestá, G. P., O. B. Brown, and R. H. Evans (1991), The annual cycle of satellite-derived sea surface temperature in the southwestern Atlantic Ocean, *J. Clim.*, 4, 457–467.
- Pollard, R., and J. Read (1989), A method for calibrating ship-mounted acoustic doppler current profilers, and the limitations of gyrocompasses, *J. Atmos. Oceanic Technol.*, 6, 859–865.
- Richardson, P. L., and T. K. McKee (1984), Average seasonal variation of the Atlantic equatorial currents from historical ship drifts, *J. Phys. Oceanogr.*, 14, 1226–1238.
- Schott, F. A., and C. W. Böning (1991), The WOCE model in the western equatorial Atlantic: Upper layer circulation, *J. Geophys. Res.*, 96, 6993–7004.
- Schott, F. A., L. Stramma, and J. Fischer (1995), The warm water inflow into the western tropical Atlantic boundary regime, spring 1994, *J. Geophys. Res.*, 100, 24,745–24,760.
- Schott, F. A., J. Fischer, and L. Stramma (1998), Transports and pathways of the upper-layer circulation in the western tropical Atlantic, *J. Phys. Oceanogr.*, 28, 1904–1928.
- Schott, F. A., M. Dengler, P. Brandt, K. Affler, J. Fischer, B. Bourlès, Y. Gouriou, R. L. Molinari, and M. Rhein (2003), The zonal currents and transports at 35°W in the tropical Atlantic, *Geophys. Res. Lett.*, 30(7), 1349, doi:10.1029/2002GL016849.
- Servain, J. M., A. J. Busalacchi, M. J. McPhaden, A. D. Moura, G. Reverdin, M. Vianna, and S. Zebiak (1998), A pilot research moored array in the tropical Atlantic, *Bull. Am. Meteor. Soc.*, 79, 2019–2031.
- Silveira, I. C. A., L. B. Miranda, and W. S. Brown (1994), On the origins of the North Brazil Current, *J. Geophys. Res.*, 99, 22,501–22,512.
- Snowden, D., and R. L. Molinari (2003), Subtropical cells in the Atlantic Ocean: An observations summary, in *Interhemispheric Water Exchange in the Atlantic Ocean*, edited by G. Goni and P. Malanotte-Rizzoli, pp. 287–312, Elsevier, Amsterdam.
- Stramma, L., and F. Schott (1999), The mean flow field of the tropical Atlantic Ocean, *Deep Sea Res., Part II*, 46, 279–303.
- Stramma, L., S. Juttl, and J. Schafstall (2005a), Water masses and currents in the upper tropical northeast Atlantic off northwest Africa, *J. Geophys. Res.*, 110, C12006, doi:10.1029/2005JC002939.
- Stramma, L., M. Rhein, P. Brandt, M. Dengler, C. Böning, and M. Walter (2005b), Upper ocean circulation in the western tropical Atlantic in boreal fall 2000, *Deep Sea Res., Part I*, 52, 221–240, doi:10.1016/j.dsr.2004.07.021.
- Urbano, D. F., M. Jochum, and I. C. A. Silveira (2006), Rediscovering the second core of the Atlantic NECC, *Ocean Modell.*, 12, 1–15, doi:10.1016/j.ocemod.2005.04.003.
- Wilson, W. D., E. Johns, and R. L. Molinari (1994), Upper layer circulation in the western tropical North Atlantic Ocean during August 1989, *J. Geophys. Res.*, 99(C11), 22,513–22,523.
- Wilson, W. E., E. Johns, and S. L. Garzoli (2002), Velocity structure of North Brazil Current rings, *Geophys. Res. Lett.*, 29(8), 1273, doi:10.1029/2001GL013869.
- Zang, D., M. J. McPhaden, and W. E. Johns (2003), Observational evidence for flow between the subtropical and tropical Atlantic: The Atlantic subtropical cells, *J. Phys. Oceanogr.*, 33, 1783–1797.

R. A. F. De Almeida, P. Nobre, and D. F. Urbano, Divisão de Modelagem e Desenvolvimento, Centro de Previsão de Tempo e Estudos Climáticos, Instituto Nacional de Pesquisas Espaciais, Rodovia Presidente Dutra KM40, Cachoeira Paulista, SP 12630-000, Brazil. (dfurbano@cptec.inpe.br)